# 15 HYDROGEOPHYSICAL METHODS AT THE LABORATORY SCALE

TY P.A. FERRÉ[1], ANDREW BINLEY[2], JIL GELLER[3], ED HILL[4], and TISSA ILLANGASEKARE[5]

[1]*University of Arizona, Hydrology and Water Resources, 1133 E. North Campus Drive, Tucson, AZ, 85721-0011 USA*

[2]*Lancaster University, Department of Environmental Science, Lancaster, LA1 4YQ, UK.*

[3]*Lawrence Berkeley National Laboratory, Earth Sciences Division, 1 Cyclotron Road, Berkeley, CA, 94720 USA*

[4]*Massachusetts Institute of Technology, Dept. of Earth, Atmospheric, and Planetary Sciences, 77 Massachusetts Ave, Cambridge, MA 02139-4307 USA*

[5]*Colorado School of Mines, Environmental Science and Engineering, 1500 Illinois St., Golden, CO, 80401 USA*

## 15.1 Unique Contributions and Challenges of Laboratory-Scale Hydrogeophysics

Hydrogeophysics relies on the inference of hydrologically important properties based on the measurement of other properties that are more easily obtained. This inference requires, first, the definition of petrophysical relationships such as the dependence of the bulk dielectric permittivity of a medium on its volumetric water content (see Chapters 4 and 9 of this volume). Second, confounding effects must be defined or controlled to allow for appropriate corrections. For example, if electrical resistance tomography (ERT) is to be used to infer water-content changes, the change in measured electrical conductivity as a function of temperature must be accounted for, or measurements must be made under isothermal conditions. Third, if the measured property or the property of interest varies within the measurement sample volume, then the manner in which the measurement method averages these heterogeneous values must be considered.

Under controlled laboratory conditions, petrophysical parameters can often be defined more completely and more accurately throughout the measurement domain than is possible under field conditions. In addition, the confounding effects of multiple properties that may affect the geophysical response can be controlled more closely than under field conditions. As a result, when applied carefully and appropriately in the laboratory, geophysical methods can produce high-resolution (in space and time), nondestructive, and inexpensive measurements to monitor transient hydrologic processes. In addition, some of these methods can be applied in entirely noninvasive modes. This final quality is of particular interest for laboratory measurements made in relatively small domains, which may be more susceptible to impacts caused by measurement devices.



*Y. Rubin and S.S. Hubbard (eds.), Hydrogeophysics*, 441–463.
© 2005 *Springer. Printed in the Netherlands.*

Despite the promise of hydrogeophysics for laboratory-based investigations, it is critical that geophysical measurements be interpreted with both hydrologic and geophysical understanding to avoid systematic errors. This chapter presents background material and case studies to demonstrate the contributions and limitations of laboratory-scale hydrogeophysics. Among the large number of geophysical methods that have been applied to laboratory studies, four are discussed here: time-domain reflectometry, x-ray tomography, electrical resistance tomography, and seismics. This is not intended to be a complete discussion of the application of geophysics at the laboratory scale, as this is too large a topic to cover in a single chapter. Rather, the purpose of this chapter is to demonstrate some of the strengths and weaknesses of geophysical methods for small-scale monitoring. Primary attention is focused on the achievable spatial and temporal resolutions of the method, the manner in which properties are averaged within the sample volume of each instrument, and the way in which hydrologic understanding should be used in designing and interpreting hydrogeophysical monitoring networks.

## 15.2 Underlying Principles of Selected Geophysical Methods

### 15.2.1 TIME DOMAIN REFLECTOMETRY (TDR)

Time domain reflectometry (TDR) is one of the most widely used geophysical methods in soil science and vadose zone hydrology. The method is used to determine the apparent dielectric permittivity of a medium based on the measured velocity of a guided electromagnetic (EM) wave. For a wide range of soils, the dielectric permittivity can be uniquely related to the volumetric water content with little or no medium-specific calibration (Topp et al., 1980).

A TDR probe (Figure 15.1) typically includes a waveguide comprised of two or three parallel metal rods. These rods range in length from 10 cm to several meters, are typically less than 1 cm in diameter, and are separated by less than 10 cm. The rods are inserted into the medium of interest using an attached nonmetallic probe handle. The handle is connected to a fast-rise-time pulse generator and an oscilloscope through a coaxial cable. An EM plane wave travels along the rods in transverse electromagnetic mode (the electric and magnetic fields are located in a plane that is perpendicular to the long axes of the rods). The wave traverses the length of the rods and is completely reflected from the ends of the rods. The two-way travel time of the wave along the rods is measured. A practical guide to the use of TDR for water-content measurement is presented by Topp and Ferré (2002), and a recent critical review of the theory and application of TDR and other related dielectric permittivity methods is presented by Robinson et al. (2003).

TDR measurements require dedicated high-frequency electronic instrumentation. However, the broad use of this method has led to the availability of commercial TDR systems. These systems are designed for laboratory and field use, and many are amenable to automated monitoring and multiplexing. With multiplexing, TDR is well suited to very rapid monitoring of the volumetric water content distribution. However,

the method is inherently intrusive because the rods are inserted into the medium of interest.

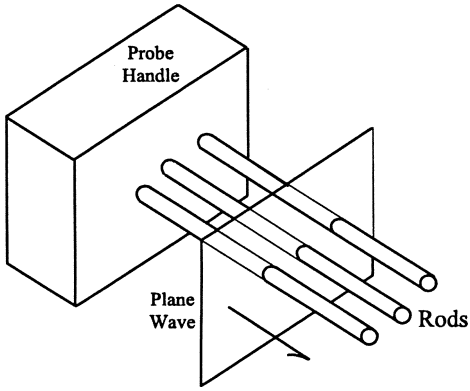


Figure 15.1. Schematic diagram of a TDR probe including the probe handle and three parallel metal rods. A guided EM plane waves travel along the rods.

### 15.2.2 ELECTRICAL RESISTANCE TOMOGRAPHY (ERT)

As described in detail in Chapter 4 of this volume, electrical resistivity varies spatially and temporally within a soil, owing to changes in porosity, saturation, fluid conductivity, temperature, and soil composition (e.g., clay content). Images of such variation within a volume of soil may thus provide useful hydrological information, particularly if these can be obtained in a noninvasive, or minimally invasive, manner. The general method of electrical resistivity imaging is now widely known as electrical resistance (or resistivity) tomography (ERT). The method has been used widely in the biomedical field (e.g., Webster, 1990; Brown, 2001) and chemical engineering (e.g., Wang et al., 2002), where it has also been referred to as electrical impedance tomography (EIT). ERT uses combinations of four-electrode measurements to derive the distribution of resistivity within a volume of interest. ERT may be applied at a wide range of spatial scales to determine hydrologic properties such as volumetric water content or solute concentration.

Adopting a four-electrode arrangement, electrical current is injected between two electrodes, and the potential difference is measured between another pair of electrodes. Figure 15.2 illustrates the approach when applied around the perimeter of a circular object, such as a soil core. Such measurements are repeated for different combinations of four electrodes, thus "scanning" different parts of the sample. It is then possible to determine the distribution of resistivity consistent with such a set of measurements. Because current flow lines are not linear, determination of the image of resistivity requires application of nonlinear inverse methods (see Chapter 5 of this volume). The distribution of resistivity is normally obtained using finite element or finite difference grid-based methods. Current flow lines are also not two-dimensional. In the schematic in Figure 15.2, measurements will be sensitive to variations in resistivity "off-plane," and thus true tomographic "slices" are not achievable with 2-D imaging. For a 64-

electrode arrangement shown in Figure 15.2, several hundred measurements are required for satisfactory image reconstruction. Using a typical low-cost multiplexed earth-resistance meter, data acquisition time may be of the order of several tens of minutes for one plane. This may limit the application of ERT for monitoring dynamic hydrological processes. Recent developments in multichannel earth-resistance meters are likely to prove valuable in studying time-varying processes in soils using ERT.

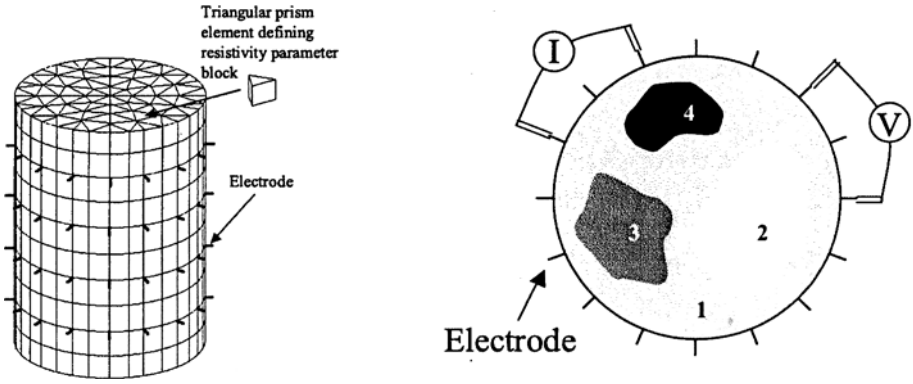


Figure 15.2. Electrical resistance tomography applied to a soil core (left). Within each horizontal slice, electrical current ($I$) is injected between two electrodes and the electrical potential ($V$) is measured between another pair of electrodes (right). The electrical conductivity distribution is then inferred within the slice.

### 15.2.3 X-RAY TOMOGRAPHY

Investigations of water content, porosity, nonaqueous phase liquid (NAPL) distributions, and NAPL mass in porous media can be accomplished through a range of different x-ray and gamma-ray attenuation techniques. For typical laboratory-scale natural-gamma and x-ray attenuation devices, the equations used for the measurement of porosities and fluid volume fractions within porous media are reviewed by Hill et al. (2002). These investigators have typically relied upon the Beer-Lambert relation,

$$\overline{N}(\varepsilon) = \Delta t I_0(\varepsilon) e^{-\rho u'(\varepsilon) l} = \Delta t I_0(\varepsilon) e^{-u(\varepsilon) l} \tag{15.1}$$

where $\overline{N(\varepsilon)}$ is the expected value of the number of observed photons at energy $\varepsilon$, $\Delta t$ is the observation time, $I_o(\varepsilon)$ is the mean photon flux at energy $\varepsilon$, $\rho$ is the material density, $l$ is a differential path length, and $u'(\varepsilon)$ and $u(\varepsilon)$ are intrinsic and linear attenuation coefficients, respectively, with $\rho u'(\varepsilon) = u(\varepsilon)$. Applying this equation with observed values of photon counts and known attenuation coefficients, one can estimate apparent fluid path lengths, masses, and/or saturations. In all cases, differences in observed photon fluxes are related to changes in the hydrologic system from a background condition. In this chapter, densities are assumed constant, so that the linear attenuation coefficient may be used to infer the intrinsic attenuation coefficient.

Typical source/detector pairs are shown in Figure 15.3. The upper diagram shows a natural gamma source coupled with a sodium iodide detector. While this is a relatively inexpensive approach, it often suffers from poor spectral resolution and relatively long counting times. The x-ray and "high-performance germanium" configuration below is more expensive, but can provide higher overall photon observation rates, better spectral resolution, and, as a result, much lower measurement times.

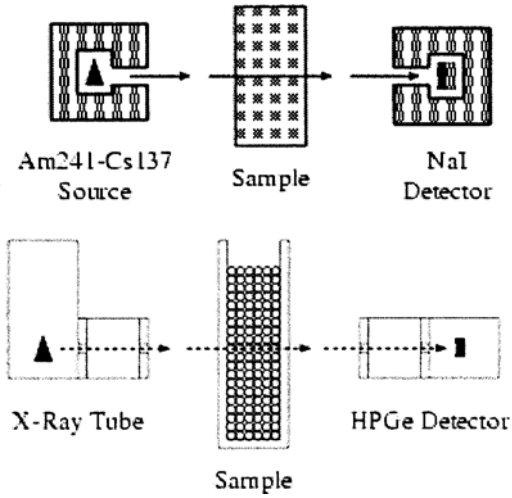


Figure 15.3. Typical source-detector configurations

In all systems, the number of photons observed tends to follow a Poisson distribution, meaning that the precision of any observation will increase with the square root of the observation time. Typical observation times (reported as detector "live" or counting times) for natural gamma systems are in the range of 100 to 500 seconds [Imhoff, 1992; Illangasekare et al., 1995], while x-ray and synchrotron sources can provide similar or better quality measurements in one to ten seconds [Imhoff et al., 1995; Okuda et al., 1996; Miller et al., 2000]. Practical issues such as motor positioning and equipment communication can increase the overall time required per location. Such time overheads can add anywhere from a few seconds to a few minutes to the total time. With a judicious choice of the number and scheduling of the sample locations, these measurement times have proven short enough to observe dynamic effects such as NAPL flow in sand-packed columns [Imhoff et al., 1995; Okuda et al., 1996; Miller et al., 2000; Hilpert et al., 2001] and dense NAPL (DNAPL) migration in large-scale tanks (Illangasekare et al., 1995). As improved electronics for photon observation and better analysis techniques (Hill et al., 2002) become available, measurement rates will increase, allowing more detailed views of DNAPL migration.

### 15.2.4 SEISMIC METHODS

The propagation characteristics of seismic waves depend upon the physical properties of the porous medium and its fluids. Chapter 8 of this volume describes the different

types of seismic waves, their attributes (such as velocity, amplitude and frequency), and applications for characterization and imaging of the shallow subsurface. Most laboratory measurements of seismic properties are one-dimensional characterizations of core samples. In-depth discussions of the concepts and considerations for experimental design can be found in texts such as Bourbie et al. (1987) and Santamarina (2001). There are very few reports in the literature of two- and three-dimensional laboratory-scale seismic imaging (Chu et al., 2001; Li et al. 2001; McKenna et al., 2001; Geller et al., 2000), but these types of systems can be beneficial for process-monitoring, particularly for changes in fluid distribution. Air and common LNAPL (light NAPL) and DNAPL contaminants have acoustic velocities and bulk moduli less than those of water. As a result, their redistribution may be visible under certain conditions from the changes in seismic waveforms measured over time.

Laboratory-based seismic investigations must be designed to use the appropriate seismic source for the scale of the measurement domain and for the spatial scale of medium heterogeneities. The transmission distance must be at least several wavelengths long. The practical physical scale of laboratory experiments (centimeters to meters) therefore defines the useable frequency range for laboratory applications. Core-scale investigations use frequencies from 100–1000 kHz, which range from one to eight orders of magnitude greater than those used for seismic field investigations. Tank-scale measurements can be made at lower frequencies. Considering the range of seismic wave velocities for geologic media (refer to Table 8.2), wavelengths at laboratory frequencies can range from millimeters to centimeters, depending upon the media, the wave type (P or S), and the measurement technique. While the scale of the measurement domain defines the minimum frequencies that can be used in the laboratory, heterogeneities control the maximum frequencies. Scattering of seismic energy can be significant for objects that have length scales greater than one-tenth of the seismic wavelength. In samples having heterogeneities near the size of a wavelength or greater, energy may be lost to scattering and diffraction when the object has an acoustic impedance contrast with the surrounding media (e.g., Santamarina, 2001; also, Chapter 8 of this volume). This can apply to both solid-phase heterogeneities, such as gravel or clay inclusions, and fluid-phase heterogeneities, created by the presence of immiscible fluid phases.

A common way to generate and detect high-frequency seismic waves is to use piezoelectric elements that expand when subjected to a voltage. This transmits a wave that is sensed as a pressure pulse and converted to a voltage at the receiver. Waveforms are typically acquired digitally, and multiple waveforms are averaged (or stacked) to improve the signal-to-noise ratio. Typical measurement times are less than one minute and depend upon the length of the waveform and the number of waveforms stacked.

Wave transmitters and receivers (or transducers) can be positioned in a variety of locations to satisfy the coverage requirements for the desired type of imaging. Proper coupling of the transducer to the media ensures energy transmission through the sample without undesirable wave-conversion effects at the contact with the sample, or fast-path transmission around the sample. Because the piezoelectric transducers must be isolated from the sample, measurement is inherently noninvasive. For time-lapse imaging,

transducer coupling must be reproducible, particularly if amplitude information is used. Transducers must also be located to avoid interference from reflections at sample boundaries.

Standard methods of seismic tomography, as described by Lo and Inderwiesen (1994), utilize the travel time of the wave and its amplitude, and invert for the two-dimensional distributions of velocity and attenuation. These methods are quite robust for low-resolution imaging, but some of the underlying assumptions do not necessarily hold in the presence of wavelength-scale heterogeneities. Development of tomographic methods to incorporate multidimensional wave propagation and full waveform inversion is an active area of research (Keers et al., 2001). Zero-offset monitoring is a straightforward method of imaging spatial and temporal changes in a sample. The zero-offset data are a subset of a tomographic dataset wherein the transmitter and receiver are directly opposite one another as they are moved vertically along the sample. The received waveforms plotted over the length of the sample provide an image of horizontally averaged properties, without waveform processing and inversion.

## 15.3 Spatial Averaging and Spatial Resolution

In forming petrophysical relationships to interpret hydrogeophysical measurements, steps are commonly taken to form homogeneous calibration samples. In contrast, most monitoring efforts are applied under conditions that give rise to spatially heterogeneous property distributions at critical times or locations, such as the time at which a wetting front reaches a measurement point or locations near the edges of NAPL pools. Correct interpretation of many hydrogeophysical measurements relies on an understanding of the concept of spatial averaging and the associated concepts of spatial sensitivity and sample volume. High-resolution laboratory measurements can be misinterpreted if the effects of spatial averaging are ignored.

### 15.3.1 SPATIAL SENSITIVITY AND SAMPLE VOLUME

The sensitivity of a measurement method can be defined as the change in the instrument response per unit change in the property of interest. The spatial sensitivity can then be considered to be a map of the change in instrument response per unit change in property of interest as a function of the location of that change. To better understand the effects of instrument design on spatial sensitivity, consider the two different configurations of electrodes shown in Figure 15.4: two circular electrodes or two parallel-plate electrodes. The electric flux density is uniform everywhere between the plate electrodes, as shown by the uniform spacing of the equipotentials. In contrast, for circular electrodes, the electric flux density is very high in the vicinity of the electrodes and lower farther from the electrodes, as shown by the nonuniform spacing of the equipotentials between the rods. As a result, a small change in the electrical conductivity at a point near one of the circular electrodes will cause a greater change in the measured electrical conductivity between the electrodes than the same conductivity change located farther from the electrodes. In contrast, a point change in conductivity at any location between the plate electrodes will have the same impact on the measured

electrical conductivity. Note that Figure 15.4 was constructed assuming that the medium properties were uniform between the electrodes; the effects of heterogeneous medium properties are discussed with reference to TDR below.

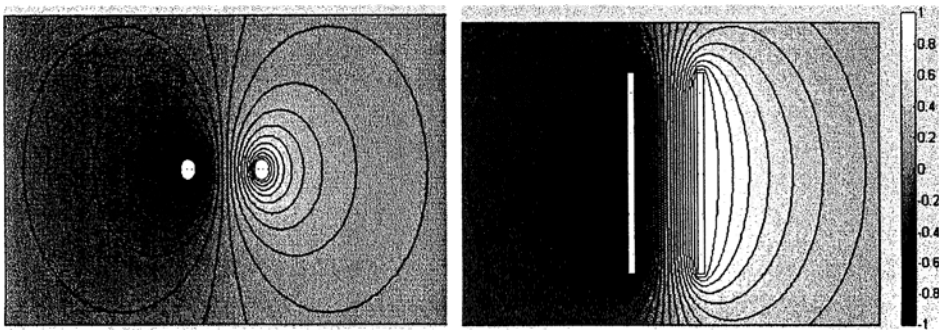


Figure 15.4. Equipotentials between two circular electrodes (left) and two plate electrodes (right) with constant potentials of 1 and –1 set on the left and right electrodes, respectively

### 15.3.2 TDR: EFFECTS OF HETEROGENEITY ON SPATIAL SENSITIVITY

Topp et al. (1982) showed experimentally that TDR measures the average water content along the rods even if the water content varies along the rods. It is more difficult to show directly how TDR responds to water-content variations in the plane perpendicular to the long axes of the rods. Knight (1992) presented an analytical expression describing the spatial sensitivity of TDR in the transverse plane if the water content is uniform. The analysis is based on the electrical potential distribution in the transverse plane. For a two-rod probe, this distribution is identical to the potential distribution around two circular electrodes, as shown in Figure 15.4. At any point in the plane, the sensitivity can be determined based on the square of the gradient of potential (Knight, 1992). As a result, the probe sensitivity is highest near the circular electrodes, especially in the region between the electrodes. In addition, if the water content is spatially uniform, the potential distribution, and therefore the sensitivity distribution, is independent of the water content.

Two approaches are commonly used to define the sample volume of an instrument. In the simplest and most common approach, measurements are made while the property of interest is varied at different distances from the instrument. The volume within which a given change in the property of interest gives rise to a measurable change in the instrument response is defined as the sample volume. While this approach gives a direct measure of the maximum volume in which a change can be sensed, it does not describe the relative contributions of the instrument response from different areas within this volume. A second approach to defining the sample volume relies on a description of the instrument spatial sensitivity.

For example, to define the sample area of TDR in the plane perpendicular to the long axis of the rods, Knight (1992) calculated the cumulative sensitivity within ellipses of varying sizes surrounding the rods. Then he identified the ellipse that contained some

percentage of the total instrument sensitivity. For TDR, the sample volume can be defined by extending this ellipse over the length of the rods. This approach offers further insight into instrument sensitivity, but because it is based on an arbitrary choice of sample area shape (e.g., an ellipse), it does not define a unique sample area (or volume). Ferré et al. (1998) introduced a unique sample area definition that identifies the minimum area containing a given fraction of the total instrument sensitivity. This is achieved by summing areas within the domain, beginning with the areas of highest sensitivity and progressing to areas of continually decreasing sensitivity. Knight et al. (1997) presented a numerical approach to analyze TDR spatial sensitivity. The unique sample areas for four TDR probes based on this analysis are shown in Figure 15.5. The origin of the plot is located at the point equidistant from the centers of the outermost rods. Each quadrant represents a different probe design. The upper left quadrant shows the 90%, 70%, and 50% sample areas of a two-rod probe with relatively small diameter rods. Because of the symmetry of the probe design, all of the remaining quadrants surrounding this probe will have the identical fractional sample areas. The lower-left quadrant represents a two-rod probe with the same rod separation as that shown above, but with a larger rod diameter. The result demonstrates that the choice of rod size has little impact on the fractional sample areas of two-rod probes. The right quadrants represent three-rod probes. The outer rod separations and rod diameters are identical to those of the two-rod probes. These results show that the fractional sample areas of three-rod probes are much smaller than those of directly comparable two-rod probes. Furthermore, the 70% of the instrument response containing the areas of highest sensitivity is located in the region immediately adjacent to the probes, which is most susceptible to disturbance during rod insertion. Based on these results, three-rod probes are only recommended when measurements must be highly localized, and then only if medium disturbance during probe placement can be minimized.

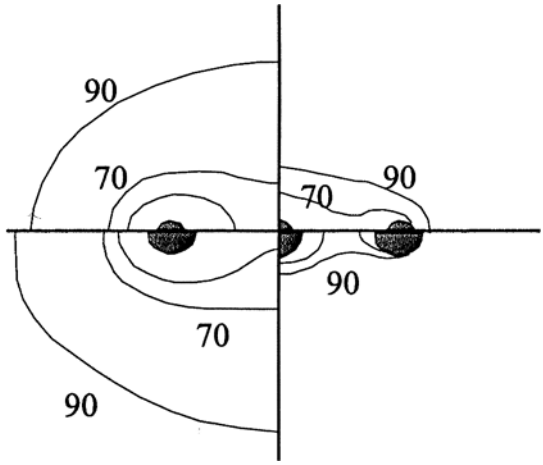


Figure 15.5. Unique fractional sample areas surrounding two-rod (left quadrants) and three-rod (right quadrants) TDR probes in a homogeneous medium. The upper and lower quadrants have the same rod separations, but smaller rods are considered in the upper quadrants. Labels show the percent of the total sensitivity contained within each contour.

Numerical analysis of TDR fractional sample areas can be applied to spatially heterogeneous media as well. Nissen et al. (2003) designed an experiment to test the effects of heterogeneous dielectric permittivity distributions on the spatial sensitivity of TDR in the transverse plane. Using multiple fluids, they achieved sharp boundaries between media of known dielectric permittivities. Two- and three-rod TDR probes were placed through the walls of a plastic box. Then, fluids (water, ethanol, oil) were added to the base of the box, causing the fluid-air interface to rise past the rods. Measurements were made continuously as the fluid level rose. At each measurement time, the height of the fluid interface was determined, allowing for the construction of a numerical model to represent the dielectric permittivity distribution. The predicted and measured dielectric permittivities showed very good agreement for horizontal two- and three-rod probes (oriented such that all probes were located in the same horizontal plane). The responses of vertical two-rod probes were also well predicted. However, for three-rod vertical probes, the results showed that the sharp dielectric permittivity contrast gave rise to two waves traveling simultaneously and at different speeds when the interface was between two of the rods. This behavior violates the assumption of plane wave propagation underlying the numerical analysis. As a result, the controlled laboratory experiments both validated the modeling approach for horizontal and vertical two-rod probes, and uncovered unexpected limitations to the use of three-rod TDR probes in heterogeneous media. The predicted dielectric permittivities were determined based on the calculated spatial sensitivities of the TDR probes for each air-fluid interface location. Therefore, this agreement provides validation of the spatial sensitivity determinations and allows for calculation of the fractional sample areas in heterogeneous media.

As the air-fluid interface rose past the TDR probe, the measured dielectric permittivity changed smoothly as a function of interface height from that of air to that of the fluid. This smoothing of the sharp interface is a function of the distributed spatial sensitivity of TDR probes. That is, when the interface is located at the probe midpoint, some of the probe sensitivity extends into each fluid. This is also true when the interface is located above or below the probe midpoint. The shape of the measured dielectric permittivity versus interface height can be explained based on the changing spatial sensitivities of the probes as a function of the dielectric permittivity distribution around the probe. The 70% and 90% sample areas for vertical two-rod probes are shown in Figure 15.6 for a series of air-water interface locations. There is significant distortion of the sample area, caused by medium heterogeneity. Specifically, most of the probe sensitivity is confined within the air until the interface reaches the upper rod. As a result, the measured dielectric permittivity is close to that of air until the interface reaches the upper rod. Once the interface passes the upper rod, the majority of the instrument sensitivity is located within the water. As a result of this changing spatial sensitivity, the most rapid change in measured dielectric permittivity occurs when the interface contacts the uppermost rod, not when the interface passes the probe midpoint. Ferré et al. (2002) show that this behavior can impact the accuracy of inversion of hydraulic properties from water-content measurements made during the advance of a wetting front.

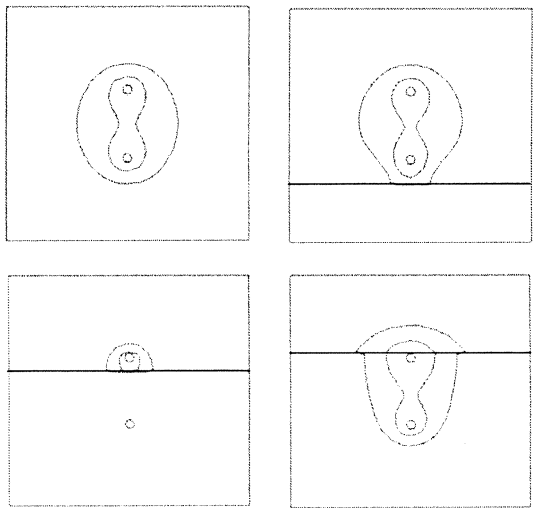

Figure 15.6. Unique fractional sample areas surrounding vertical two-rod TDR probes as water rises past the probe. The horizontal line shows the air-water interface: air overlies water in all cases. The outer contours contain 90% of the probe sensitivity and the inner contours contain 70%.

### 15.3.3 EFFECTS OF SAMPLE HOLDERS ON X-RAY METHOD AVERAGING

Spatial averaging of observations is largely determined by the beam geometry of the attenuation device employed. Typically, parameters such as the geometry of the x-ray focal spot (Knoll, 1979), the construction of the natural-gamma source, and the size and arrangement of collimators at the source and detector ends are used to control the beam geometry. In all instruments, the number of photons observed at a detector is a weighted average of the contributions of all the possible paths that the photons could travel from the source or sources to the detector.

To illustrate the physics of photon attenuation averaging, we will consider a simplified example involving a single source and detector combination as shown in Figure 15.3. Assuming that all photons travel in paths parallel to the z-axis, that the photon detector has perfect quantum efficiency, and that the contribution of Compton-scattered photons is negligible, the average rate of photon observation at the detector for any particular photon energy $\varepsilon$ is the weighted average of photon flux over the projected beam area, according to:

$$\overline{N}(\varepsilon) = \int_{t=0}^{\Delta t} \int_{x=0}^{\Delta x} \int_{y=0}^{\Delta y} I_0(\varepsilon, x, y, t) e^{-\int_{z=z_d}^{z_s} \mu(\varepsilon, x, y, z, t) dz} \, dydxdt \qquad (15.2)$$

where $z_s$ and $z_d$ are the source and detector locations (with the $z$ axis parallel to the beam), $\Delta x$ and $\Delta y$ are the beam height and width, $\Delta t$ is the observation time, $I_0(x, y, t)$ is the photon flux (production rate) per unit area at the source, $\upsilon(e, x, y, z, t)$ is the spatially and temporally distributed attenuation coefficient of the material(s) placed within the

beam path, and $\overline{N}(\varepsilon)$ is the average number of photons observed at the detector. If photon production rate at the source is uniform over the area of the beam, then the following simplification may be applied as

$$I_0(\varepsilon, x, y, t) = \frac{1}{\Delta x \Delta y} I_0(\varepsilon, t). \tag{15.3}$$

The instrument response is an attenuation-weighted average of the photon observation rate. Since we are interested in employing this photon attenuation effect to measure densities or fluid saturations within porous media, it is useful to investigate how the attenuation average is related to a fluid mass average or a fluid volume average over the identical domain.

First, we consider a cuvette of constant and known thickness placed within the beam path, as shown in Figure 15.3. This technique is a commonly used method for the calibration of photon attenuation devices. Initially, the cuvette is scanned while it contains only air, which has a negligible attenuation coefficient. Then the cuvette is filled with water (or some other fluid with a known photon attenuation behavior) and scanned a second time. According to the Beer-Lambert equation (15.2), there is an exponential relationship between the thickness (or "path length") of the material and the number of observed photons. With this knowledge, one can perform calibration experiments to determine the extinction rate of the material (the "attenuation coefficient," $\mu$) by simultaneously measuring path lengths and observed photon rates. Conversely, one can use previously calibrated attenuation coefficients and observed photon rates to measure material thicknesses.

In this case, the sample has a flat and uniform fluid thickness relative to the photon beam. It can be readily shown that the integrals along the temporal and all three spatial dimensions in Equation 15.2 can be reduced to a single instance of the Beer-Lambert equation. Thus, for a flat and constant absorber geometry, the attenuation weighted average is identical to a mass or a volume average of the fluid over the projected beam area (that is, the volume of the beam). However, for more complicated attenuator geometries, the equivalence between attenuation, mass, and volume averages does not, in general, hold. To prove there is a bias between attenuation and mass or volume averages, consider the hypothetical case of a flat plate, which has an "eggcrate"-like pattern of flat bumps on one side. The projected thickness, $l$, of this object at any x, y-coordinate can be specified as

$$l(x, y) = \bar{l} + \Delta l \operatorname{sgn}\left( \sin\left( \frac{2n\pi xy}{\Delta x \Delta y} \right) \right), \tag{15.4}$$

where $\bar{l}$ is the average plate thickness, $\Delta << \bar{l}$ is the protrusion length of the square "bumps," and the "sgn" function is defined as

$$\operatorname{sgn}(a) = \begin{matrix} -1, a < 0 \\ 0, a = 0 \\ 1, a > 0 \end{matrix} . \quad (15.5)$$

Given that the attenuation coefficient for the plate is constant over space and time, and that the plate geometry and the photon source strength are constant over time, Equations 15.2, 15.3, and 15.4 can be applied over the projected beam area to obtain:

$$\overline{N}(\varepsilon) = \frac{\Delta t I_0(\varepsilon)}{2}\left[e^{-\left(\bar{l}+\Delta l\right)\mu(\varepsilon)} + e^{-\left(\bar{l}-\Delta l\right)\mu(\varepsilon)}\right], \quad \ldots \quad (15.6)$$

which expresses the average number of observed photons at a particular energy $\varepsilon$ as a function of both the average plate thickness $\bar{l}$ and the length $\Delta$ of the square "bumps" on its surface.

Applying either a mass or a volume average to the plate over the beam volume, one can readily show that the average thickness of the plate is $\bar{l}$,. since the high and low regions would exactly cancel each other out. For the attenuation-weighted case, the representative or "average" length ($l$=$\hat{l}$ ) as measured using observations of photon counts for a single energy would be from Equations 15.1 and 15.6:

$$\hat{l} = \bar{l} - \frac{1}{\mu(\varepsilon)} \ln\left(\frac{1}{2} e^{-\Delta l \mu(\varepsilon)} + \frac{1}{2} e^{\Delta l \mu(\varepsilon)}\right), \quad (15.7)$$

which gives a consistently negative bias. By examining the term within the logarithm, one can prove that

$$\begin{matrix} \hat{l} < \bar{l}, \Delta l \neq 0 \\ \hat{l} = \bar{l}, \Delta l = 0 \end{matrix} . \quad (15.8)$$

That is, the measured (attenuation-averaged) length will be consistently smaller than the mass-averaged or volume-averaged length for any non-zero "bump height" in this analysis. This result agrees with our previous description of a flat plate geometry and hints at a more general bias in measurements involving fluid saturations in porous media—since, as we have shown, an attenuation average over the beam area is not necessarily the same as a mass or volume average. A good example of such bias occurring within a laboratory experiment is the monitoring of oil saturations within a rock core sample or soil packed within a glass column (Imhoff, 1992, 1995). Both of these experimental domains have cylindrical geometries typically on the order of a few centimeters in diameter. If one uses a sufficiently small beam of radiation aligned to create a perpendicular intersection with the centerline of the cylindrical domain, then the assumption of a "flat" beam intersection area is probably justified. However, if the beam is not aligned with the center of the cylinder, or if the beam width approaches or exceeds the width of the cylindrical domain, then the bias can be large. In such cases, an attenuation measurement of the fluid mass at a point within the column may be dramatically less than the true mass within the beam intersection volume. In general, an

experimentalist has no prior knowledge of the fluid distributions, so he or she cannot estimate the expected path length variations over the projected beam area as described by Equation 15.2. Thus it is, in general, impossible to derive *a priori* corrections. Furthermore, even if the fluid geometry were known, Equation 15.2 is itself only an approximation. This suggests that care should be taken to form experimental conditions that lead to near-uniform thicknesses for all measurements.

## 15.4 Sample Density

The spatial resolution of hydrologic properties and processes that can be achieved with geophysical methods depends on both the sample volume of each measurement and the spacing of measurements. As described in the preceding sections, the sample volume of each measurement depends on the instrument design and on the distribution of materials within the domain. Measurement spacing is defined by an investigator based on the expected relevant scale of the hydrologic process of interest, often in balance with a time constraint imposed by the time required for each measurement. The tradeoff between spatial and temporal resolution is most critical when geophysical methods are applied to monitor transient hydrologic processes. For example, this tradeoff between the measurement times, the number of locations, and the measurement accuracy/precision is often a critical practical concern for gamma- and x-ray systems, since observation times can be significant (1–500 s per location is typical) relative to the experimental time scales.

### 15.4.1 SAMPLE DENSITY EFFECTS ON X-RAY DNAPL MASS ESTIMATION

To demonstrate the impact of the choice of sample density on hydrologic interpretations, consider the estimation of DNAPL mass in a two-dimensional flow cell using an x-ray system (Moreno-Barbero, in submission). The container used had internal dimensions of approximately 25 cm long by 18 cm high by 2 cm thick (Figure 15.7). The cell was wet-packed with two uniform quartz sands: a coarse-grained sand to form the rectangular inclusion and a finer-grained sand surrounding it. A total of 27.0 ± 0.1 grams of tetrachloroethylene (PCE), dyed with a small mass of SudanIV to increase visibility, was slowly injected through a port in the back of the tank to create the high-saturation pool. Following injection, the tank was scanned with the x-ray system to measure the PCE mass at 256 locations (Figure 15.7). Because the box was wet-packed, the wet/dry differencing method for the x-ray measurement of the spatial distribution of porosities could not be applied. While having an unknown porosity distribution makes it difficult to determine DNAPL saturations precisely, it is not an impediment to the measurement of DNAPL masses. Assuming that the DNAPL has a constant density, each measurement is interpreted in terms of a representative DNAPL path length (or "effective thickness") at each measurement location. Statistical analyses of the error variance for this data set suggests that, at individual points, PCE path lengths were measured with a standard error of about 0.2 mm. Over the entire domain, the mass balance as calculated from all interpolated x-ray data from four complete scans is 27.7 ± 0.3 grams. This is in excellent agreement (less than 2.5% error) with the known total

injected mass. Further examination of the results shows very high gradients in the PCE saturation between adjacent measurement locations at the lateral edges of the pool. In contrast, little variation in saturation exists within the pool. It is likely that a large fraction of the error in total mass estimation results from interpolation between the measurement points spanning the edge of the pool. A redesigned experiment could place measurement points closer together at the edges of the pool to capture the highly spatially variable saturations in this region; the lower limit on measurement spacing would be defined by the dimensions of the beam used.

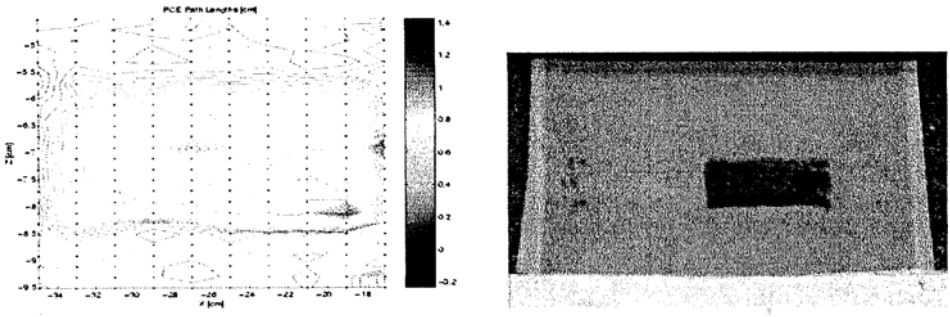

Figure 15.7. (left) A DNAPL pool (PCE dyed w/SudanIV) within a coarse sand inclusion; (right) DNAPL path lengths as measured by x-ray attenuation. The interior dimensions of the tank are approximately 25 cm long by 18 cm high by 2 cm thick.

## 15.5 Instrument Averaging

Every hydrogeophysical method has an associated sample volume (or sample volumes). This sample volume places a primary control on the achievable spatial resolution of the method. In addition, this sample volume describes the volume over which the medium properties are averaged by the instrument. That is, the measured property may depend on the distribution of the property of hydrologic interest within the sample volume. If this is the case, then there is a nonunique relationship between the measured property and the volume-average of the property of interest in the sample volume. This requires knowledgeable interpretation of hydrogeophysical results, as well as geophysical insight, to design effective hydrogeophysical measurement networks.

### 15.5.1 EFFECTS ON SEISMIC NAPL PROFILING

The distribution of immiscible fluid phases in porous media is extremely sensitive to how they are emplaced, and can be highly irregular, or patchy. Not only will values of fluid saturation vary with sample volume, but immiscible fluid distribution within a given sample volume can range from evenly dispersed to patchy. For measurement of NAPL saturation changes with *P*-waves at the laboratory scale, the millimeter- to centimeter-long seismic wavelengths are often of similar length scales as NAPL blobs or patches. Under these conditions, the seismic *P*-wave signature may respond to both the average medium properties, as well as to the geometry of NAPL distribution. The

results from *P*-wave monitoring of a controlled NAPL spill in a laboratory-scale tank illustrate some of the issues that arise with measurement averaging.

An experiment was performed in a 60 cm diameter by 75 cm tall tank, with 3 cm diameter acrylic wells just inside the vessel wall for crosswell *P*-wave data acquisition. The *P*-wave source was placed in one well and the receiver in a second well on the opposite side of the tank. The bottom two-thirds of the tank was packed with a coarse, subrounded 0.85 mm to 1.7 mm grain diameter quartz sand, over which a 25 cm thick layer of 44 to 88-micron diameter glass beads was placed to form a capillary barrier. Then, n-Dodecane, dyed red, was injected from the bottom of the water-saturated tank, such that the lighter-than-water NAPL migrated upward, leaving residual NAPL segments along its flow paths, and accumulating as a lens in the coarse sand below the capillary barrier. The source and receiver were moved over the depth of the tank in increments of 1 cm, and the transmitted *P*-wave was recorded at each station, for the water-saturated tank. Over the course of three days, 6.7 L of n-dodecane was injected into the tank from the bottom. Displaced water was recovered from the top of the tank and the *P*-wave scan was repeated.

The record of the waveforms of each zero-offset scan collected before and after NAPL injection (Figure 15.8) shows a change in grayscale intensity (amplitude) associated with the first arrival of the *P*-wave. In zero-offset scans, the received waveforms represent horizontally averaged properties. The piezoelectric source produced waves with a central frequency of about 90 kHz, resulting in an approximately 2 cm wavelength. The reference scan (the water-saturated tank) in Figure 15.8a shows attenuation and diffraction caused by the glass bead/sand interface. This interface is not sharp, and includes a transitional region, indicated by the pair of dashed black lines in the figure, of about 2–3 cm where the smaller diameter beads fill the pore space of the coarse sand. In the postinjection scan (Figure 15.8b), negligible waveform changes occur in the glass bead layer, compared to the reference scan. In the 15 cm below the glass bead layer, delayed travel times and amplitude reductions of 60 to 95% result from the presence of the NAPL lens. The highly attenuated first-arrival times within the lens are indicated by a dashed white line. Below the lens, the residual NAPL causes amplitude reductions of 1 to 30% and changes in diffraction patterns. Amplitude decreases caused by the presence of NAPL are much greater than the variability of the water-saturated sand.

Following the post-injection scan, the three-dimensional distribution of the NAPL was determined by excavation. A thin-walled brass grid covering the horizontal cross-sectional area of the tank was pressed into the sand pack to guide the excavation of 5 cm × 5 cm × 5 cm samples. The NAPL volume in the samples taken from the scanning plane were measured by extracting the dyed NAPL into a known volume of clean n-dodecane and measuring the resulting dye concentration with a UV spectrophotometer. The measured porosity of each sample was used to calculate the NAPL saturation. No NAPL was detected within the glass bead layer (Figure 15.9a). Most of the NAPL accumulated in the top 15 cm of the coarse sand, where NAPL saturations ranged from 32% to 81% of the pore space. NAPL saturations are lower near the top of the lens, because of the smaller pore sizes where smaller glass beads partially fill the coarse sand

pores. Part of the lens was excavated by freezing layers over the entire cross section of the tank with liquid nitrogen, without the brass grid, which facilitated the removal of large volumes of NAPL. This measurement produced horizontally averaged saturation values shown in Figure 15.9b. The other saturation values below the lens in Figure 15.9b were calculated from the 2-D distributions measured in Figure 15.9a. Below the lens, saturations range from 0 to 16%, with maximum values corresponding to the depths of maximum amplitude change seen in Figure 15.9c at 58 and 63 cm.

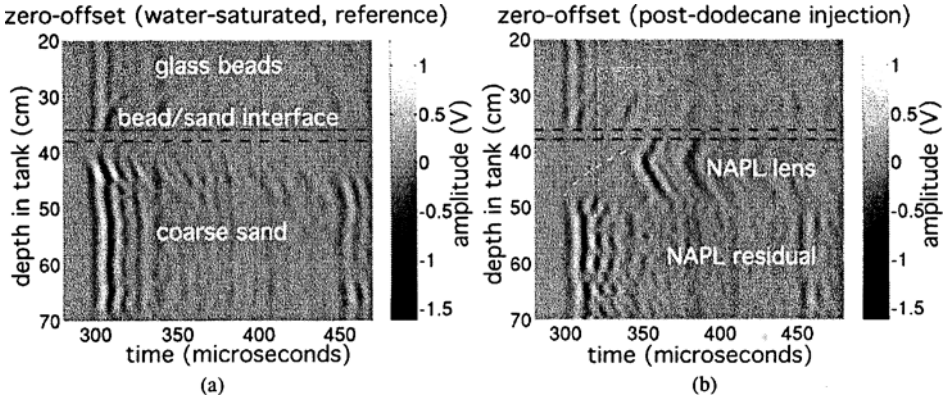


Figure 15.8. Comparison of zero-offset (source and receiver at same depths) *P*-wave travel time and amplitude data through tank for (a) water-saturated conditions (or reference scan), and (b) after injection of n-Dodecane from tank bottom. The arrival time of the *P*-wave is indicated by the first change in gray tone, moving along the time axis. The presence of the NAPL lens can be seen in the significant delay in arrival time (indicated by the dashed white line) and reduced amplitude over the 15 cm below the glass bead/sand interface. The NAPL residual below the lens causes velocity and amplitude changes relative to the reference scan. Data from Geller et al. (2000).

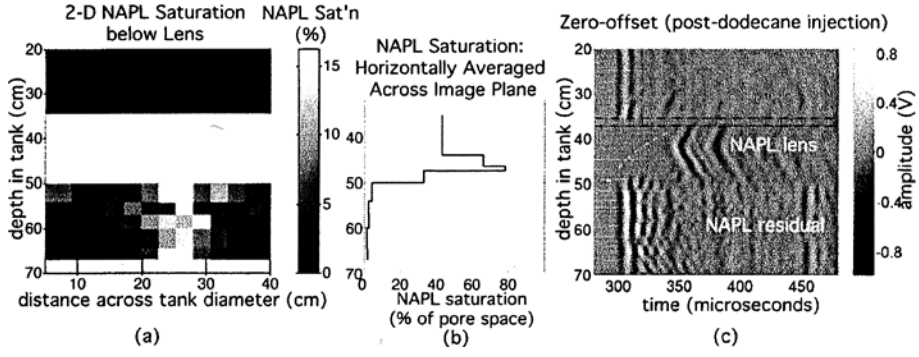


Figure 15.9. NAPL saturation in the scanning plane from excavation, compared with the postinjection zero-offset *P*-wave scan. The measured NAPL distribution corresponds to the *P*-wave signature change. (a) NAPL saturation below the NAPL lens, measured from samples excavated in 5 cm × 5 cm × 5 cm sections. (b) Horizontally averaged NAPL saturation across the image plane. The lens was excavated by freezing layers of sand with liquid nitrogen. Samples below the lens are calculated from the 2-D distributions in (a). (c) The post-injection scan. This amplitude scan has higher gain than in Figure 15.8b. Data from Geller et al. (2000).

Through the NAPL lens, the first-arrival time decreases with depth as NAPL saturation decreases. The ray path traveled by the *P*-wave may be affected by the complex liquid distribution within the lens and the glass-bead/sand interface. However, if the ray paths of the first arrivals through the lens are directly across the tank, then these data show an increase in *P*-wave velocity (the ratio of distance traveled to travel time) with decreasing NAPL saturation. This trend is consistent with column-scale measurements that showed that *P*-wave velocity decreased almost linearly with increasing NAPL saturation (Geller and Myer, 1995). The amplitudes within the region of the lens do not change significantly (seen by the constant gray-scale intensity in Figure 15.9c), while the average NAPL saturation changes from 81% to 32% (Figure 15.9b). This suggests a nonlinear relationship between saturation and attenuation. Towards the middle of the lens, the NAPL distribution is expected to be more homogeneous throughout the horizontal cross section than near the bottom of the lens. At the bottom of the lens, patches of water-saturated media occur between sections occupied by NAPL, which may be more attenuating compared to the same volume of NAPL evenly distributed throughout the cross section. This is consistent with other observations and analyses—Geller (1995); Seifert et al. (1998); Cadoret et al. (1998)—where increased energy attenuation occurs in the presence of irregular and patchy distributions of immiscible fluids compared to lower attenuation for more homogeneous fluid-phase distributions.

This experiment shows that attenuation is much more sensitive than velocity to the presence of NAPL. The effect of NAPL distribution on *P*-wave attenuation suggests that NAPL patches may scatter seismic energy at laboratory-scale frequencies. However, the dependence of *P*-wave attenuation on NAPL geometry indicates that while increased attenuation may be the more sensitive indicator of the presence of NAPL, it cannot be used to quantify the value of saturation. On the other hand, *P*-wave velocity may be used to estimate NAPL saturation because of the linearity of velocity response to NAPL saturation. The determination of valid relationships for *P*-wave velocity as a function of NAPL saturation in unconsolidated sands is an area of ongoing research. However, the available theories are consistent with a near-linear relationship under constant loads. Gassman's (1951) equations for pore-fluid substitution estimate the bulk modulus of a mixture as a function of its constituent solid and fluid properties, and have been applied to the problem of hydrocarbon detection in oil reservoirs (e.g., Mavko and Mukerji, 1998; Dominico, 1976). Geller and Myer (1995) predicted measured *P*-wave velocities through sands saturated with varying fractions of water and NAPLs using effective composition laws by Kuster and Toksöz (1974) and the average of the liquid properties. However, fitting the data to the prediction required lower porosities than were experimentally measured. It is possible that amplitude data may prove useful for screening for the presence of NAPL, velocity data may allow for quantitative analysis of NAPL saturations, and combined amplitude and velocity data could describe both the saturation and the distribution of NAPL.

## 15.6 Time-Lapse Monitoring

One of the most significant advantages of geophysical methods for hydrologic monitoring is their ability to measure with little or no disruption to the system under investigation. This allows for multidimensional monitoring of transient processes, which is highly limited, if not impossible, with conventional methods. The use of ERT for multidimensional, transient hydrologic monitoring is more advanced than other methods. An example of the use of ERT for monitoring solute transport through a structured column is presented.

### 15.6.1 BENEFITS OF ERT TIME-LAPSE MONITORING

ERT has limited value in characterizing soil or rock structure from static images and will certainly be unable to resolve millimeter scale macropore or fracture features. ERT may, however, be applied to study the spatial changes of pore fluid content over time and thus elucidate flow pathways within the system. By imaging changes in resistivity in an area or volume, ERT can be used to infer the proportion of pore volume contributing to flow, without necessarily imaging individual flow paths (as illustrated earlier for larger scale studies in Chapter 14 of this volume. Henry-Poulter et al. (1993), Binley et al. (1996a,b), Henry-Poulter (1996), and Olsen et al. (1999) have applied ERT to studies of solute transport in soil cores. This section presents some of the results and findings of these studies.

Binley et al. (1996a) used ERT to infer mobile and immobile pore fractions during the transport of a solute through a 32 cm diameter, 46 cm long undisturbed soil column. Four electrode planes were used, each with 16 electrodes, in a similar arrangement to that in Figure 15.2. A selection of ERT results at the four electrode planes monitored are shown in Figure 15.10, displayed as percentage changes in electrical conductivity relative to the pre-tracer conditions. Each horizontal plane is discretized into 104 triangular pixels, at each of which a resistivity value was computed for each frame.

During the early stages of the tracer test, changes in electrical conductivity are localized to a small volume of the soil core. After 19 hours, changes near the outflow are minor and yet breakthrough of the tracer was apparent. This is likely to be a result of transport through localized connected macropores within the core, which ERT is unable to resolve. Note that if one assumes purely advective transport at the pore-water velocity obtained from the model fit to the breakthrough curve, then the tracer "front" at 19 hours should be only approximately 6 cm from the base; and yet significant changes 28 cm from the base are clearly evident in the ERT images. After 34 hours, a marked zone of changes in soil conductivity is seen in the ERT image plane close to the outflow, at a time when the breakthrough curve showed a period of near-constant effluent concentration with time. This may result from early breakthrough and near-steady-state conditions within a small pore volume of highly transmissive macropores. After approximately 60 hours, the breakthrough curve showed a marked second rising limb of the curve, consistent with the increasing contributing volume observed in the ERT images near the outflow at 34 hours. After 94 hours, this volume has grown somewhat, but localized high conductivity changes are still significant. At 97 hours, a low-

conductivity tracer was injected into the base of the column. Subsequent ERT images show that this low-conductivity tracer also influences the same zones that were influenced by the high-conductivity tracer. Other areas in which tracer has perhaps migrated laterally are slow to change.

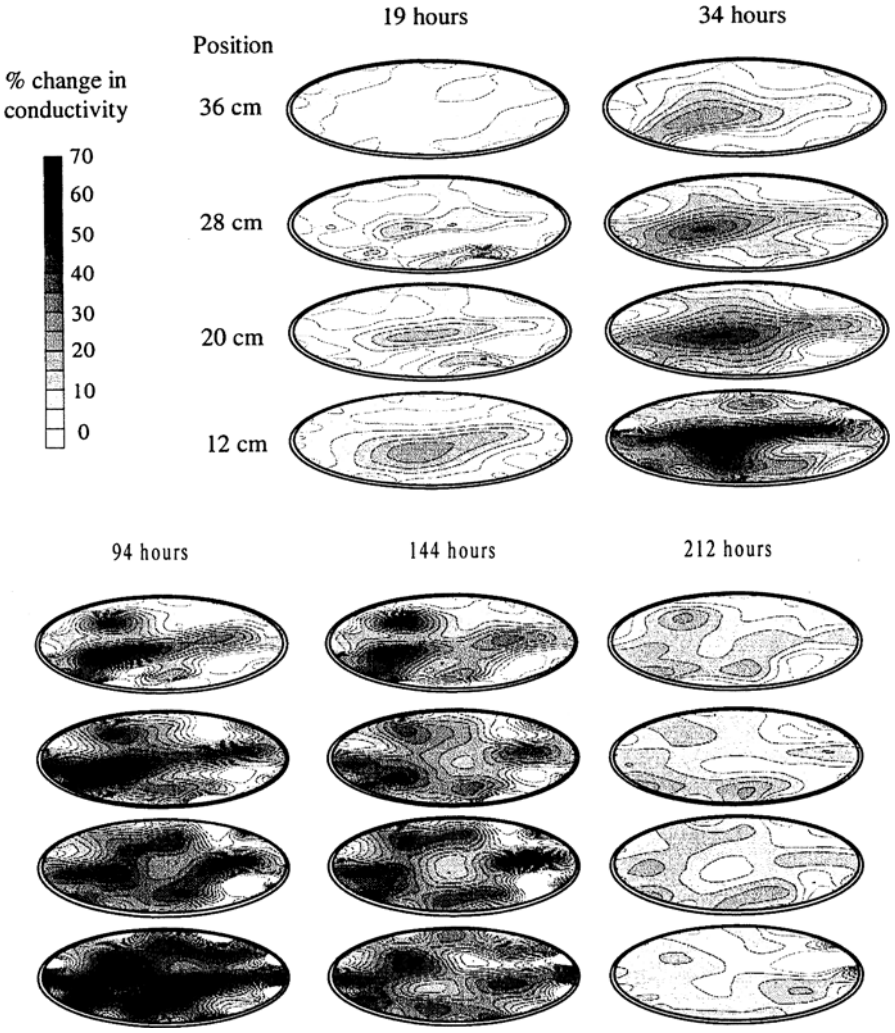


Figure 15.10. Sequence of ERT images of soil-core sections at four positions from the base of the core. Changes in electrical conductivity caused by saline tracer applied at base of core are shown. The high electrical conductivity tracer ends after 97 hours, followed by a low-electrical-conductivity tracer injection.

Binley et al. (1996a) introduced the simple concept of analyzing the ERT images as equivalent to results from pore water samplers located within the soil core (see also Slater et al., 2000; Slater et al., 2002). Figure 15.11 shows changes in conductivity, expressed as a relative concentration, for three pixels in the ERT plane 12 cm from the

tracer injection (Figure 15.2). There is a marked difference between the three responses. Pixels 50 and 80 show symmetrical behavior, albeit with different magnitudes, similar to the observed effluent breakthrough curve (see Binley et al. [1996a] for details). Pixel 103, in contrast, shows a marked rise in conductivity until ~25 hours after tracer injection, after which time a comparably steady response is seen. Such behavior supports the notion of two distinct phases seen in the outflow breakthrough curve.

Dye staining of the core (see also Binley et al. [1996b] for application to different soil columns) revealed some consistency with the ERT results. However, most dye staining was confined to a very small fraction of the soil core volume. Such staining probably indicated the most transmissive fraction of the core and underestimates the true contributing pore fraction. Using 3-D ERT imaging of two soil columns, Olsen et al. (1999) extended the work of Binley et al. (1996a) by modeling the tracer breakthrough for two soil columns using transfer function techniques. With such models, Olsen et al. (1999) were able to quantify the significance of a preferential transport component in each system. Their ERT results clearly show supporting evidence of preferential flow in a soil column, with a significant bypass flow inferred from tracer breakthrough analysis.

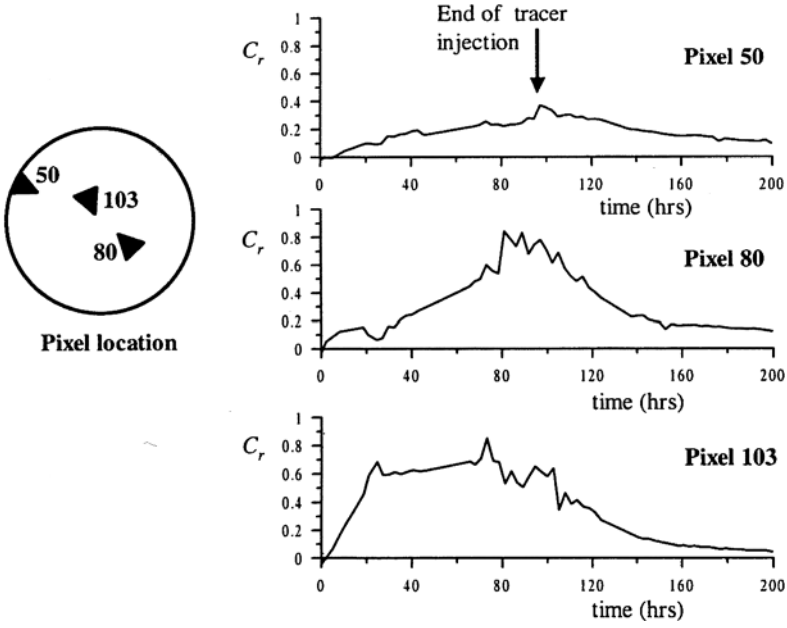


Figure 15.11. ERT pixel breakthrough curves for three selected locations in a plane 12 cm from tracer injection

## 15.7 Potential Contributions of Laboratory Hydrogeophysics When Properly Applied

Hydrogeophysical methods can make substantial contributions to laboratory studies of fluid flow and mass transport. These methods can offer minimally invasive, nondestructive, rapid, automated measurements that are relatively inexpensive compared with chemical analyses. These qualities are essential for conducting multidimensional monitoring of transient hydrologic processes. Case studies of the application of TDR, x-ray methods, seismic methods, and ERT are shown to demonstrate the unique abilities of hydrogeophysical methods for laboratory investigations. However, further discussion of case studies presents potential limitations to the use of hydrogeophysical methods. Specifically, TDR, x-ray, and seismics case studies demonstrate the need for the effects of spatial averaging within the measurement volume to be considered when making hydrologic interpretations. An x-ray case study is used to demonstrate the importance of the choice of sample locations when designing a hydrogeophysical monitoring network. Finally, a seismics case study demonstrates that many hydrogeophysical methods provide multiple measurements that can be used for hydrologic interpretation. Intelligent use of these measures, together with hydrologic understanding, can extend the use of hydrogeophysics for hydrologic investigations.

## References

Binley, A., S. Henry-Poulter, and B. Shaw, Examination of solute transport in an undisturbed soil column using electrical resistance tomography, *Water Resour. Res., 32*(4), 763–769, 1996a.

Binley, A., B. Shaw, and S. Henry-Poulter, Flow pathways in porous media: Electrical resistance tomography and dye staining image verification, *Measurement Science and Technology, 7*(3), 384–390, 1996b.

Bourbie, T., O. Coussy, and B. Zinszner, *Acoustics of Porous Media,* Gulf Publishing Company, Houston, TX, 1987.

Brown, B.H., Medical impedance tomography and process impedance tomography: A brief review, *Measurement Science & Technology, 12*(8), 991–996, 2001.

Cadoret, T., G. Mavko, and B. Zinszner, Fluid distribution effect on sonic attenuation in partially saturated limestones, *Geophysics, 63*, 154–160, 1998.

Chu, D., D. Tang, T.C. Austin, A.A. Hinton, and R.I. Arthur, Jr., Fine-scale acoustic tomographic imaging of shallow water sediments, *IEEE Journal of Oceanic Engineering*, *26*(1), 70–83, 2001.

Dominico, S.N., Effect of brine-gas mixture on velocity in an unconsolidated sand reservoir, *Geophysics*, *41,* 882–894, 1976.

Ferré, T.P.A., H.H. Nissen, and J. Šimunek, The effect of the spatial sensitivity of TDR on inferring soil hydraulic properties from water content measurements made during the advance of a wetting front, *Vadose Zone Journal*, *1*, 281–288, 2002.

Ferré, P.A., J.H. Knight, D.L. Rudolph, and R.G. Kachanoski, The sample area of conventional and alternative time domain reflectometry probes, *Water Resour. Res., 34*(11), 2971–2979, 1998.

Gassman, F., Uber die elasttizitat poroser medien, *Vier. der Natur Gesellschaft*, *96,* 1–23, 1951.

Geller, J. T., M. B. Kowalsky, P. K. Seifert and K. T. Nihei, Acoustic detection of immiscible liquids in sand, *Geophysical Research Letters*, *27*(3), 417–420, 2000.

Geller, J.T. and L.R. Myer, Ultrasonic imaging of organic liquid contaminants in unconsolidated porous media, *Journal of Contaminant Hydrology*, *19*(3), 1995.

Henry-Poulter, S.A., An investigation of transport properties in natural soils using electrical resistance tomography, Unpublished PhD Thesis, Lancaster University, U.K., 1996.

Henry-Poulter, S.A., M.Z. Abdullah, A.M. Binley and F.J. Dickin, Electrical impedance tomography of tracer migration in soils, In: *Computational methods and Experimental Measurements IV, Vol 1: Heat and*

*Fluid Flow,* by Brebbia and Carlomagno, eds., Computational Mechanics Publications, pp. 101–115, 1993.

Hill III, E.H., L.L. Kupper, and C.T. Miller, Evaluation of path-length estimators for characterizing multiphase systems using polyenergetic x-ray absorption, *Soil Science*, *167*(11), 703–719, 2002.

Illangasekare, T.H., E.J. Armbruster III, and D.N. Yates, Non-aqueous-phase fluids in heterogeneous aquifers—Experimental study, *Journal of Environmental Engineering*, 121(8), 571- 579, 1995.

Imhoff, P.T., Dissolution of a nonaqueous phase liquid in saturated porous media, PhD Thesis, Princeton University, 1992.

Imhoff, P.T., S.N. Gleyzer, J.F. McBride, L.A. Vancho, I. Okuda, and C.T. Miller, Cosolvent-enhanced remediation of residual dense nonaqueous phase liquids: Experimental investigation, *Environmental Science & Technology*, *29*(8), 1966–1976, 1995.

Keers, H., D.W. Vasco and L.R. Johnson, Viscoacoustic crosswell imaging using asymptotic waveforms, *Geophysics, 66*(3), 861–870, 2001.

Knight, J.H. Sensitivity of time domain reflectometry measurements to lateral variations in soil water content, *Water Resour. Res.*, *28,* 2345–2352, 1992.

Knoll, G.F., *Radiation Detection and Measurement,* John Wiley and Sons, New York, NY, 1979.

Kuster, G.T., and M.N. Toksöz, Velocity and attenuation of seismic waves in two-phase media; Part I—Theoretical formulations, *Geophysics*, *39*(5), 587–606, 1974.

Li, X., L.R. Zhong, and L.J. Pyrak-Nolte, Physics of partially saturated porous media: Residual saturation and seismic-wave propagation, *Annual Review of Earth & Planetary Sciences*, *29*, 419 –460, 2001.

Lo, T-w., and P.L. Inderwiesen, *Fundamentals of Seismic Tomography,* Geophysical Monograph Series, #6, Society of Exploration Geophysicists, Tulsa, OK, 1994.

Mavko, G., and T. Mukerji, Bounds on low-frequency seismic velocities in partially saturated rocks, *Geophysics*, *63*(3), 918–924, 1998.

McKenna, J., D. Sherlock, and B. Evans, Time-lapse 3-D seismic imaging of shallow subsurface contaminant flow, *Journal of Contaminant Hydrology*, *53*, 133–150, 2001.

Miller, C.T., E.H. Hill, III, and M. Moutier, Remediation of DNAPL-contaminated subsurface systems using density-motivated mobilization. *Environmental Science & Technology*, *34*(4), 719–724, 2000.

Moreno-Barbero, E., Evaluation of partitioning inter-well tracer tests for character-ization of DNAPL pools, PhD Dissertation, Colorado School of Mines, Golden, Colorado, in submission.

Nissen, H.H., P.A. Ferré, and P. Moldrup, The transverse sample area of two- and three-rod time domain reflectometry probes: dielectric permittivity *Water Resour. Res., 38*(10), No. 1289, 2003.

Okuda, I., J.F. McBride, S.N. Gleyzer, and C.T. Miller, An investigation of physicochemical transport processes affecting the removal of residual DNAPL by nonionic surfactant solutions. *Environmental Science & Technology*, *30*(6), 1852–1860, 1996.

Robinson D.A., S.B. Jones, J.M. Wraith, D. Or, and S.P. Friedman, A review of advances in dielectric and electrical conductivity measurement in soils using time domain reflectometry, *Vadose Zone Journal*, *2*, 444–475, 2003.

Santamarina, J.C., *Soils and Waves*, in collaboration with K.A. Klein and M.A. Fam, John Wiley & Sons, Ltd., Chichester, West Sussex, England, 2001.

Seifert, P.K., J.T. Geller and L.R. Johnson, Effect of P-wave scattering on velocity and attenuation in unconsolidated sand saturated with immiscible liquids, *Geophysics*, *63*(1), 161–170, 1998.

Slater, L., A. Binley, W. Daily and R. Johnson, Cross-hole electrical imaging of a controlled saline tracer injection, *J. Appl. Geophysics*, *44,* 85–102, 2000.

Slater, L., A. Binley, R. Versteeg, R., G. Cassiani, R. Birken, and S. Sandberg, A 3D ERT study of solute transport in a large experimental tank, *J. Appl. Geophysics*, *49*(4), 211–229, 2002,.

Olsen, P.A., A. Binley, S. Henry-Poulter, and W. Tych, Characterising solute transport in undisturbed soil cores using electrical and x-ray tomographic methods, *Hydrological Processes*, *13,* 211–221, 1999.

Topp, G.C., J.L. Davis, and A.P. Annan, Electromagnetic determination of soil water content: measurement in coaxial transmission lines, *Water Resour. Res., 16*, 574–582, 1980.

Topp, G.C., J.L. Davis and A.P. Annan, Electromagnetic determination of soil water content using TDR: I. Applications to wetting fronts and steep gradients, *Soil Sci. Soc. Am. J.*, *46,* 672–678, 1982.

Topp, G.C., and P.A. Ferré, eds., Water content measurement methods, In: *Methods of Soil Analysis,* American Society of Agronomy, 2002.

Wang, M, W. Yin and N. Holliday, A highly adaptive electrical impedance sensing system for flow measurement, *Measurement Science & Technology, 13*(12), 1884–1889, 2002.

Webster, J.G., ed., *Electrical Impedance Tomography*, Adam Hilger, Bristol, England, 1990.